



## Abstract

Currently, there is no airborne in-situ method to reconstruct with high fidelity the instantaneous elevation of a dynamically rough surface of a turbulent flow. This work proposes a new holographic method that reconstructs the elevation of a 1-D rough water surface from airborne acoustic pressure data. This method can be implemented practically using an array of microphones deployed over a dynamically rough surface or using a single microphone which is traversed above the surface at a speed that is much higher than the phase velocity of the roughness pattern. In this work, the theory is validated using synthetic data calculated with the Kirchhoff approximation and a finite difference, time domain method over a number of measured surface roughness patterns. The proposed method is able to reconstruct the surface elevation with a sub-millimetre accuracy and over a representatively large area of the surface. Since it has been previously shown that the surface roughness pattern reflects accurately the underlying hydraulic processes in open channel flow (e.g. [Horoshenkov, et al, J. Geoph. Res.,118(3), 18641876 (2013)]), the proposed method paves the way for the development of new non-invasive instrumentation for flow mapping and characterization that are based on the acoustic holography principle.

PACS: 43.20.Ye, 43.30.Hw, 43.28.Gq

Keywords: Acoustic scattering, roughness, dynamic surface, inverse method

# I Introduction

Understanding the spatial and temporal hydraulic changes in rivers and other types of open channels is of paramount importance for predicting flood risk, sediment movement and consequent morphological change. Understanding the spatial and temporal variability of flows has become a core element in assessing the water quality and ecological status of rivers (EU Water Framework Directive (WFD)). However, there is a significant shortcoming in our ability to monitor these flows at sufficient temporal and spatial resolution particularly during extreme events because there is no technology that can be deployed rapidly to accurately map the hydraulic and topographical information of rivers at a reach scale. Although attempts have been made to measure the dynamic surface roughness pattern underwater (e.g. [1, 2]), there is still a lack of real time airborne methods to measure the instantaneous surface elevation with sub-millimeter accuracy and at a very high temporal resolution. This information is of great importance for us to advance the existing theoretical link between the free surface behaviour and the underlying turbulent flow structures which carry information about the flow and sediment bed. This link can be used to study the changes in the turbulent flow structures and velocity depth profile remotely for a range of open channel flows in the laboratory and in the field using an array of acoustic sensors deployed on a large scale, e.g. with a swarm of unmanned aerial vehicles (UAV).

The main focus of this paper is to present a new method based on acoustic boundary integral equations and a pseudo-inverse technique applied to a matrix based equation to recover the instantaneous elevation of a dynamically rough surface at sub-millimeter accuracy, high temporal resolution and a representatively large spatial scale. In particular, this numerical approach enables us to study the acoustic

55 scattering from an inhomogeneous roughness that supports multiple scales.

56 The paper is organized in the following manner. Section II presents the underlying  
57 theory of acoustic scattering. This theory is then used in combination with the matrix  
58 inversion method which is described in Section III. Section IV presents the results  
59 of the application of the proposed inversion method to the acoustic pressure data  
60 which were predicted with the standard Kirchhoff approximation and with the finite  
61 differences, time domain method. The conclusions are drawn in Section V.

## 62 II Scattering of acoustic waves from a rough sur- 63 face

64 Let us consider a semi-infinite space in Cartesian coordinate system  $Oxyz$  bounded  
65 by rough surface  $S$  which mean plane  $S_0$  coincide with  $Oxy$  coordinate plane. Spatial  
66 scales and distribution of surface elevation  $\zeta(x)$  are assumed to be arbitrary within  
67 the validity range of the proposed method and in this paper both deterministic  
68 and random profiles are tested. In order to simplify the numerical calculations, it  
69 is assumed that the surface is uniform in  $Oy$ -direction and the acoustic source is a  
70 directional line source which directivity pattern  $A(x, z)$  is defined in Section IV. This  
71 makes the stated problem one dimensional. The main axis of the far-field directivity  
72 pattern is inclined at the angle  $\psi_0$  with respect to the  $Ox$  axis and it is aligned with  
73 the centre of coordinates. The coordinates of the source and receiver are defined  
74 by  $(x_1, z_1)$  and  $(x_2, z_2)$ , respectively. The source emits a continuous harmonic wave  
75  $\exp(-i\omega t)$  with angular frequency  $\omega$  and constant amplitude in time.

76 In this paper the roughness is defined by the dynamic behaviour of the water flow  
77 free surface. To maintain harmonic dependence on time, as suggested above, it is

78 assumed that the roughness is frozen over a short time period at which the complex  
79 acoustic pressure of the scattered harmonic wave needs to be measured. This is true  
80 because the speed of sound in air  $c_0 = 340$  m/s is much faster than the maximum  
81 phase velocity  $U = U_0 + c_p$  at which the surface roughness pattern on the flow surface  
82 of a typical shallow water river with the mean depth  $h$  will propagate, i.e.  $c_0 \gg U$ .  
83 Here  $U_0$  denotes the flow velocity and  $c_p = \sqrt{gh}$  is the phase velocity of the gravity  
84 waves,  $g$  is the gravity.

85 In this paper the scattering from a rough surface is approximated by the tangent  
86 plane approximation as suggested in [3]. We assume that the surface is rigid which is  
87 a good approximation for the case when sound propagates in air above a dynamically  
88 rough water surface, e.g. free surface of a turbulent open channel flow. The approx-  
89 imation is based on Kirchhoff method and principles of geometrical optics (e.g. [4]),  
90 and is valid if local curvature radius  $a$  of the rough surface is much greater than the  
91 acoustic wavelength  $\lambda = 2\pi/k$ , where  $k$  is wavenumber of the acoustic wave. For the  
92 diffraction on a sphere, this condition can be stated in the following form

$$\sin \psi \gg \frac{1}{(ka)^{1/3}}, \quad (1)$$

93 where  $a$  is a radius of the sphere locally inscribed in rough surface. The condition in  
94 eq. (1) can be relaxed to [5]

$$\sin \psi > \frac{1}{(ka)^{1/3}}, \quad (2)$$

95 so that the Kirchhoff approach remains accurate for the incident angles far from the  
96 low grazing angles. In this paper condition (2) is used in the numerical simulation  
97 to define the surface.

98 Assuming that the distances from the source  $R_1$  and receiver  $R_2$  to a given point  
99 on the mean surface (see Figure 1) are much greater than the acoustic wavelength  
100 and using the Kirchhoff method, the scattered acoustic pressure can be approximated

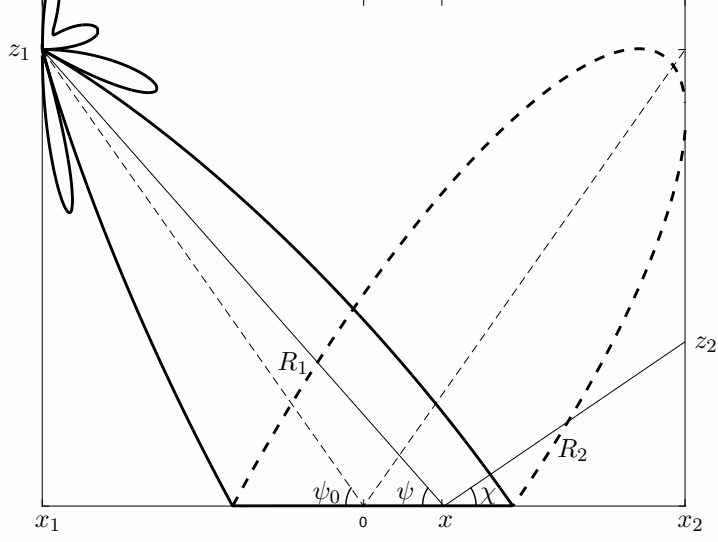


Figure 1: The geometry of the acoustic problem of rough surface scattering.

by [3, 6]

$$p(x_2, z_2) = -\frac{i}{2\pi k} \int_{S_0} \frac{A(x)}{\sqrt{R_1 R_2}} \exp[ik(R_1 + R_2) - iq_z \zeta(x)] \left[ q_z - q \frac{\partial \zeta(x)}{\partial x} \right] dx, \quad (3)$$

where  $\zeta(x)$  is surface elevation and

$$q_z = k \left( \frac{z_1}{R_1} + \frac{z_2}{R_2} \right), \quad (4)$$

$$q = -k \left( \frac{x_1 - x}{R_1} + \frac{x_2 - x}{R_2} \right), \quad (5)$$

$$R_1 = \sqrt{(x - x_1)^2 + z_1^2}, \quad (6)$$

$$R_2 = \sqrt{(x - x_2)^2 + z_2^2}. \quad (7)$$

Assuming that the surface is smooth,  $\partial \zeta(x)/\partial x \ll 1$ , equation (3) can be simplified

to

$$p(x_2, z_2) = -\frac{i}{2\pi k} \int_{S_0} \frac{A(x)}{\sqrt{R_1 R_2}} \exp[ik(R_1 + R_2) - iq_z \zeta(x)] q_z dx. \quad (8)$$

104 If the profile of the surface  $\zeta(x)$  is known than the integral in equation (8) can be  
 105 solved numerically. However, the surface in the above integral is assumed to be  
 106 unknown and it is the acoustic pressure in the left hand side which is known from  
 107 experiments. This formulates an inversion problem where the variable  $\zeta(x)$  needs to  
 108 be recovered from the available acoustic pressure data.

### 109 III Matrix inverse method

110 In order to invert the surface elevation  $\zeta(x)$  it is proposed to use a numerical approach  
 111 to solve integral equation (8). For this purpose the integral is discretised over the  
 112 surface  $S_0$  with the  $M$  uniform spatial elements  $\Delta x = x_{m+1} - x_m$ ,  $m = 1, \dots, M$   
 113 and approximated by the sum over these elements. It is noted that the size of the  
 114 element  $\Delta x$  has to be at least five times smaller than the acoustic wavelength  $\lambda$ [5]  
 115 (i.e.  $\Delta x < \lambda/5$ ). The scattered acoustic pressure at the receiver position  $(x_2, z_2)$  can  
 116 be approximated by

$$p(x_2, z_2) = -\frac{i}{2\pi k} \sum_{m=1}^M \frac{A(x_m)}{\sqrt{R_{1,m}R_{2,m}}} \exp[ik(R_{1,m} + R_{2,m}) - iq_{z,m}\zeta(x_m)] q_{z,m}\Delta x, \quad (9)$$

117 where all the terms with the index  $m$  are defined at points  $x_m$ ,  $m = 1, \dots, M$  on the  
 118 surface  $S_0$ . Equation (9) can be rewritten in the form of a scalar product of two  
 119 vectors

$$p(x_2, z_2) = \mathbf{D}_M \mathbf{E}_M, \quad (10)$$

where

$$\mathbf{D}_M = \left\{ -\frac{i}{2\pi k} \frac{A(x_m)}{\sqrt{R_{1,m}R_{2,m}}} \exp[ik(R_{1,m} + R_{2,m})] q_{z,m}\Delta x \right\}_{m=1, \dots, M}, \quad (11)$$

$$\mathbf{E}_M = \{\exp[-iq_{z,m}\zeta(x_m)]\}_{m=1, \dots, M}. \quad (12)$$

120 In order to retrieve surface profile  $\zeta(x)$  it is necessary to have acoustic pressure data  
 121 recorded at more than one receiver positions that the acoustic pressure vector  $\mathbf{P}$   
 122 with  $N$  elements can be formed. With multiple receiver positions defined by the  
 123 coordinates  $(x_{2,n}, z_{2,n})$ ,  $n = 1, \dots, N$ , equation (10) needs to be converted into the  
 124 matrix form in order to apply the matrix inversion.

125 One way of deriving the matrix form is to isolate the unknown elevation of the  
 126 rough surface  $\zeta(x)$  at the points  $x_m$ ,  $m = 1, \dots, M$  for all receiver positions in one  
 127 single vector  $\mathbf{E}_M$ . In doing so it is assumed that for fixed index  $m$  the variability of  
 128  $q_{z,mn}$ ,  $n = 1..N$  with respect to the position on the surface is negligible in the vicinity  
 129 of the specular point defined by the angle  $\psi_0$  as shown in Figure 1. This gives

$$\mathbf{P}_{N \times 1} = \mathbf{H}_{N \times M} \mathbf{E}_{M \times 1}, \quad (13)$$

130 where the elements of the matrix  $\mathbf{H}_{N \times M}$  are defined by

$$h_{mn} = \left\{ -\frac{i}{2\pi k} \frac{A(x_{mn})}{\sqrt{R_{1,mn}R_{2,mn}}} \exp[ik(R_{1,mn} + R_{2,mn})] q_{z,mn} \Delta x \right\}_{m=1, \dots, M, n=1, \dots, N} \quad (14)$$

131 and unknown vector  $\mathbf{E}_{M \times 1}$  is given by equation (11) with  $q_{z,m}$  defined by the receiver  
 132 positioned at the specular angle  $\psi_0$ . The form of equation (13) is identical to that  
 133 used in inverse frequency response function (IFRF) techniques with  $\mathbf{H}_{N \times M}$  repre-  
 134 senting transfer matrix for an array of microphones and vector  $\mathbf{E}_{M \times 1}$  representing  
 135 velocity potentials on the surface [10]. This allows us to apply previously developed  
 136 techniques to recover surface profile.

137 It is practical to assume that the number  $M$  of unknown points on the surface is  
 138 greater than the number of receivers  $N$  ( $M > N$ ). However this leads to an under-  
 139 determined system of equations which may result in an ill-conditioned matrix and a  
 140 non-unique inverse solution to problem stated in equation (13). In order to invert



matrix  $\mathbf{H}_{N \times M}$  in equation (13) it is proposed to use a pseudo-inverse method based on the singular value decomposition technique (SVD) (e.g. [7]). Applied to matrix  $\mathbf{H}_{N \times M}$  this gives

$$\mathbf{H}_{N \times M} = \mathbf{U}_{N \times N} \mathbf{S}_{N \times M} \bar{\mathbf{V}}_{M \times M}^T, \quad (15)$$

where  $\mathbf{U}_{N \times N}$  and  $\mathbf{V}_{M \times M}$  are unitary matrices (defined by  $\mathbf{A} \bar{\mathbf{A}}^T = \mathbf{I}$ ),  $\mathbf{S}_{N \times M}$  is a diagonal matrix with nonnegative elements arranged in the descending order of smallness,  $\bar{\mathbf{A}}$  stands for complex conjugate and  $\mathbf{A}^T$  denotes matrix transpose. In order to apply pseudo-inverse techniques and decrease computational time, in this paper the truncated form of matrices  $\mathbf{S}$  and  $\mathbf{V}$  in equation (15) was used so that

$$\mathbf{H}_{N \times M} = \mathbf{U}_{N \times N} \mathbf{S}_{N \times N} \bar{\mathbf{V}}_{N \times M}^T. \quad (16)$$

Applying the SVD to equation (13) and using the definition of the unitary matrix the unknown vector  $\mathbf{E}_{M \times 1}$  can be expressed in the following form

$$\mathbf{E}_{M \times 1} = \mathbf{V}_{M \times N} \mathbf{S}_{N \times N}^{-1} \bar{\mathbf{U}}_{N \times N}^T \mathbf{P}_{N \times 1}, \quad (17)$$

where  $\mathbf{S}_{N \times N}^{-1}$  indicates the matrix inverse. The matrix  $\mathbf{S}_{N \times N}$  may contain small order elements resulting in singular values in the inverted matrix  $\mathbf{S}_{N \times N}^{-1}$ . In order to regularize ill-conditioned matrix and to filter the singular elements from the inverse matrix it is proposed to use the Tikhonov regularization technique (e.g. [10] and [8]) that gives

$$\mathbf{E}_{M \times 1} = \mathbf{V}_{M \times N} \mathbf{S}_{\beta, N \times N}^{-1} \bar{\mathbf{U}}_{N \times N}^T \mathbf{P}_{N \times 1}, \quad (18)$$

where  $\mathbf{S}_{\beta, N \times N}^{-1} = [\mathbf{S}_{N \times N} + \beta^2 \mathbf{S}_{N \times N}^{-1}]^{-1}$  and  $\beta$  is the regularization parameter. In order to adjust parameter  $\beta$  we used the generalised cross validation (GCV) technique. This technique requires to minimize the following function

$$F(\beta) = \frac{r_{\beta}^2}{\text{Tr} \left( \mathbf{I}_{N \times N} - \mathbf{U}_{N \times N} \mathbf{S}_{N \times N} \mathbf{S}_{\beta, N \times N}^{-1} \bar{\mathbf{U}}_{N \times N}^T \right)^2}, \quad (19)$$

159 in which  $r_\beta$  is the residue defined by  $l^2$ -vector norm

$$r_\beta = \left\| \left( \mathbf{I}_{N \times N} - \mathbf{U}_{N \times N} \mathbf{S}_{N \times N} \mathbf{S}_{\beta, N \times N}^{-1} \bar{\mathbf{U}}_{N \times N}^T \right) \mathbf{P}_{N \times 1} \right\|. \quad (20)$$

160 The argument (phase) of each element of vector  $\mathbf{E}_{M \times 1}$  provides information about  
 161 the surface elevation. In order to retrieve the phase from matrix equation (18)  
 162 the complex natural logarithm is applied element-wise to the results of the matrix  
 163 product. This yields

$$\mathbf{Q}_{\zeta_{M \times 1}} = -\Im[\text{Ln}(\mathbf{E}_{M \times 1})], \quad (21)$$

164 where

$$\mathbf{Q}_{\zeta_{M \times 1}} = \{q_{z,m} \zeta(x_m)\}_{m=1,\dots,M}, \quad (22)$$

165 with  $\Im(< \cdot >)$  representing imaginary part of the natural logarithm. It is noted that  
 166 application of Ln in equation (21) is restricted to the case then  $-\pi < q_{z,m} \zeta(x_m) < \pi$   
 167 that enables us to uniquely define the elements of the vector  $\mathbf{Q}_{\zeta_{M \times 1}}$ . This condition  
 168 holds in the vicinity of a specular point defined by the angle  $\psi_0$  and fails as distance  
 169 between specular point and  $x_m$ ,  $m = 1, \dots, M$  increases. The discretized roughness  
 170 profile  $\{\zeta_m\}$  at the points  $\{x_m\}$  can then be deduced as

$$\{\zeta_m\}_{m=1,\dots,M} = \left\{ \frac{i \text{Ln}(e_m)}{q_{z,m}} \right\}_{m=1,\dots,M}, \quad (23)$$

171 where  $e_m$  is an element of the vector  $\mathbf{E}_{M \times 1}$ .

172 The fact that the proposed inversion largely depends on the proximity of a surface  
 173 point to the specular point leads to the idea of replacing the directional source with  
 174 simple monopole with a unit amplitude. As a result, the elements of the matrix  
 175  $\mathbf{H}_{N \times M}$  can be simplified to

$$h_{mn} = \left\{ -\frac{i}{2\pi k} \frac{\exp[ik(R_{1,mn} + R_{2,mn})]}{\sqrt{R_{1,mn} R_{2,mn}}} q_{z,mn} \Delta x \right\}_{m=1,\dots,M, n=1,\dots,N}. \quad (24)$$

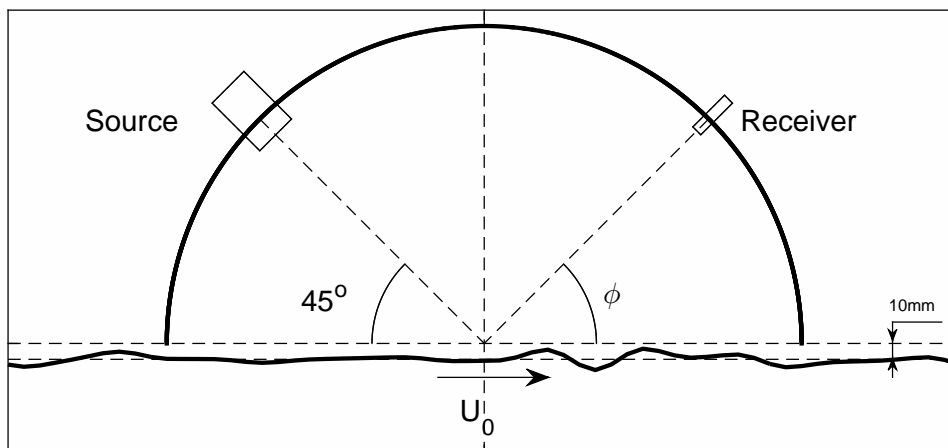


Figure 2: The acoustic setup used to reconstruct the rough surface in the numerical experiment.

176 This reduces input data to geometrical parameters defined by the position of source  
 177 and receivers with respect to the surface  $S_0$  and data recorded on the array of re-  
 178 ceivers.

## 179 IV Results

180 In this paper, validation of the proposed inversion method (equation (23)) is based on  
 181 two sets of synthetic data generated using the Kirchhoff integral and Finite Difference  
 182 Time Domain (FDTD). The former demonstrates the implementation of the proposed  
 183 inverse technique and the latter shows application of this technique to independent  
 184 set of data obtained in order to retrieve unknown surface profile.

## 185 A Simulated roughness

186 In this section the acoustic pressure scattered by the rough surface was modelled with  
 187 the Kirchhoff integral (equation (8)). In order to reconstruct the surface elevation it  
 188 was proposed to use an array of  $N = 121$  receivers arranged on a circular arch with the  
 189 radius of  $R = 0.4$  m as illustrated in Figure 2. The receivers and source are positioned  
 190 on the opposite sides of the arch. The arch is suspended at  $d = 0.01$  m above the  
 191 mean surface of water,  $S_0$ , and the centre of the arch coincides with the centre of  
 192 Ox axis. The source was installed at the angle of  $\psi_0 = 45^\circ$  and its coordinates were  
 193  $(R \cos \psi_0, R \sin \psi_0 + d)$ , where  $d$  is vertical distance of the circular arch base to the  
 194 plane  $S_0$ . The position of receivers is defined by  $(-R \cos \phi, R \sin \phi + d)$ , where  $\phi$   
 195 varies from  $15^\circ$  to  $75^\circ$  with  $0.5^\circ$  resolution that produces 121 receiver positions. The  
 196 sound source emitted a continuous harmonic wave at  $f = 43$  kHz and its directivity  
 197 pattern was defined by

$$A(\theta) = \frac{J_1(ka \sin \theta)}{ka \sin \theta}, \quad (25)$$

198 where  $a = 0.02$  m is the radius of the source aperture. The position of the receivers  
 199 was characterized by the angle  $\phi$  which was taken from the horizontal line. The  
 200 number of the receivers in the array,  $N$ , and the adopted geometry were consistent  
 201 with that used in the experiments reported by Nichols [9]. Increasing the number  
 202 of receivers may result in more singular values and it may lead to a more unstable  
 203 inverse solution. Decreasing the number of the receivers may lead to a poorer spatial  
 204 resolution of the surface elevation and higher ambiguity.

205 In the calculations reported in this section the 1-D rough surface  $\zeta(x)$  was sim-  
 206 ulated with the Fourier series containing random phase and amplitudes assigned in

207 accordance with the typical characteristics of gravity-capillary waves [11]. This gives

$$\zeta(x) = \sigma \sum_n C_n \cos(K_n x + \tau_n), \quad (26)$$

208 where  $\sigma$  is the standard deviation of the rough surface elevation (mean roughness  
209 height),  $K_n$  is wavenumber in the surface roughness spatial spectrum,  $\tau_n$  is phase  
210 which value is randomly generated and amplitude  $C_n$  is defined by the correlation  
211 function of the waves of which the surface roughness pattern is composed and it is  
212 proportional to the wavelength  $l_n$  of the  $n$ -th harmonic in the Fourier expansion so  
213 that

$$C_n \sim \left(\frac{2\pi}{l_n}\right)^{\alpha/2}. \quad (27)$$

214 In particular the amplitude of each term in the Fourier expansion is linked to the  
215 power spectrum slope defined by the power of  $\alpha = -4$  [12]. The surface elevation  
216 constructed with this kind of spatial spectrum supported multiple scales ranging  
217 from 8 mm to 115 mm and satisfied the condition (2) on the validity of Kirchhoff  
218 approximation. The standard deviation of the surface is set to  $\sigma = 1\text{mm}$ .

219 Figure 3(a) shows the surface elevation simulated with the Fourier series us-  
220 ing the range of spatial wavelengths of  $8\text{mm} < l_n < 115\text{ mm}$  and compared with  
221 surface elevation reconstructed with the proposed inversion method. This figure  
222 also shows the absolute error in the surface reconstruction which was calculated as  
223  $\epsilon_\zeta(x) = |\zeta_p(x) - \zeta_m(x)|$ , where  $\zeta_p(x)$  is the predicted surface elevation and  $\zeta_m(x)$  is  
224 the measured surface elevation. The inversion was applied to the surface interval  
225 containing  $M = 3000$  surface points that included the specular reflection point and  
226 its vicinity. It can be seen from the data presented in Figure 3 that the range of  $x$   
227 for which the surface roughness reconstruction could be achieved was limited by the  
228 position of the specular reflection point which was in the range of  $-0.1\text{ m} < x < 0.1$   
229 m. In particular, this is illustrated in Figure 3(b) where the absolute error of the

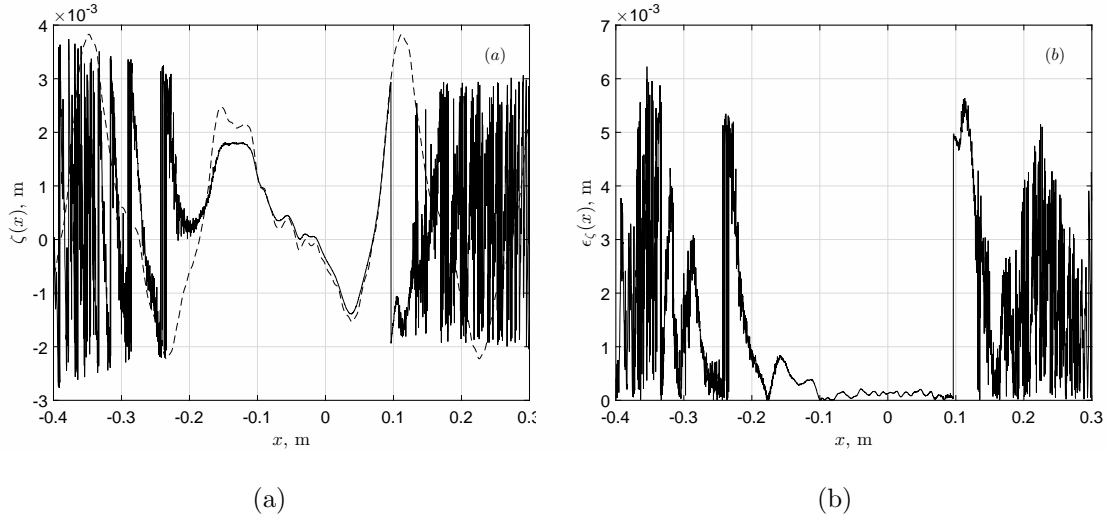


Figure 3: (a) An example of the surface realization,  $\zeta(x)$ , (dashed line) used in equation (8) and its reconstruction from the Kirchhoff approximation (solid line) based on equation (23). (b) Absolute error of the reconstructed surface.

230 surface reconstructed within this interval is limited and does not exceed 0.22 mm  
 231 which is considerably smaller than the maximum roughness height of 2.5 mm. The  
 232 root mean square error for this range does not exceed 0.12 mm that is 12% of the true  
 233 mean roughness height. in this analysis the root mean square error was calculated  
 234 as

$$\epsilon_{rms} = \sqrt{\frac{1}{N} \sum_{n=1}^N [\zeta_p(x_n) - \zeta_m(x_n)]^2}, \quad (28)$$

235 where the deduced surface elevation  $\zeta_p(x_n)$  and measured surface elevation  $\zeta_m(x_n)$   
 236 are taken at the point  $x_n$ .

237 The regularization parameter  $\beta$  was selected in accordance with equation (19).  
 238 Figure 4 illustrates the variation of the GCV function  $F$  for the reconstruction process  
 239 for the surface shown in Figure 3(a). The parameter  $\beta$  is small ( $\beta \sim 10^{-12}$ ) and  
 240 defines the threshold below which equation (18) becomes unstable. It increases with

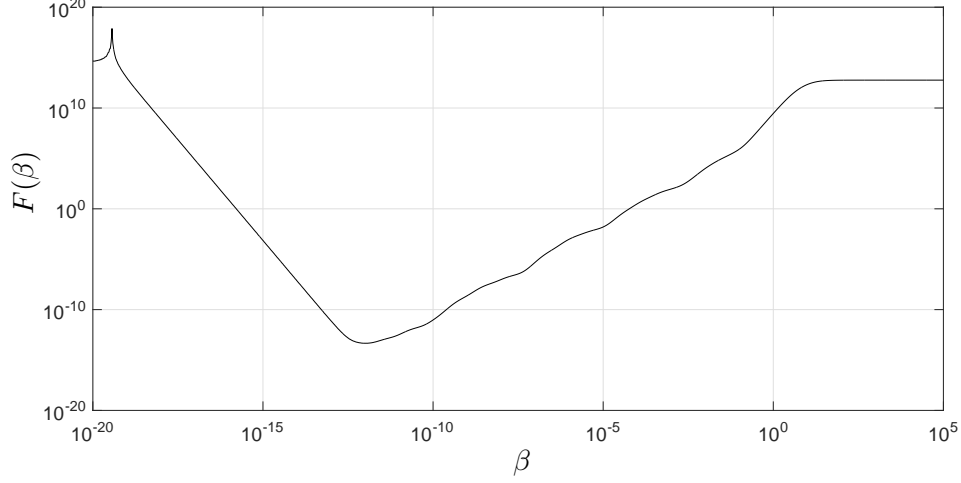


Figure 4: An example of the behaviour of the function  $F(\beta)$  for the range of  $10^{-20} < \beta < 10^5$ .

the decrease in the number of receivers causing the inversion process to become more unstable.

In order to understand the range of scales which can be recovered with equation (18) we compared the power spectrum of the surface roughness for a representative number of realizations obtained by varying randomly phase with the amplitudes of the Fourier expansion (equation (26)). The power spectrum was calculated by applying the Hanning window and Fourier transform to the original and recovered surface elevation data for each of the surface realization. It was then averaged over all the surface realizations. It was found that the average power spectrum converges to the true mean value to within 1% provided that at least 100 surface realizations were used. The average power spectrum inverted with the proposed method follows the slope  $\alpha = -4$  defined by equation (27) for  $K < 2000$ . This corresponds to the roughness wavelength of  $l_n \approx 3.4$  mm which is comparable to the receiver separation of 3.5 mm. For the spectrum of larger scales (centimetre scale) when  $K < 1000$  the

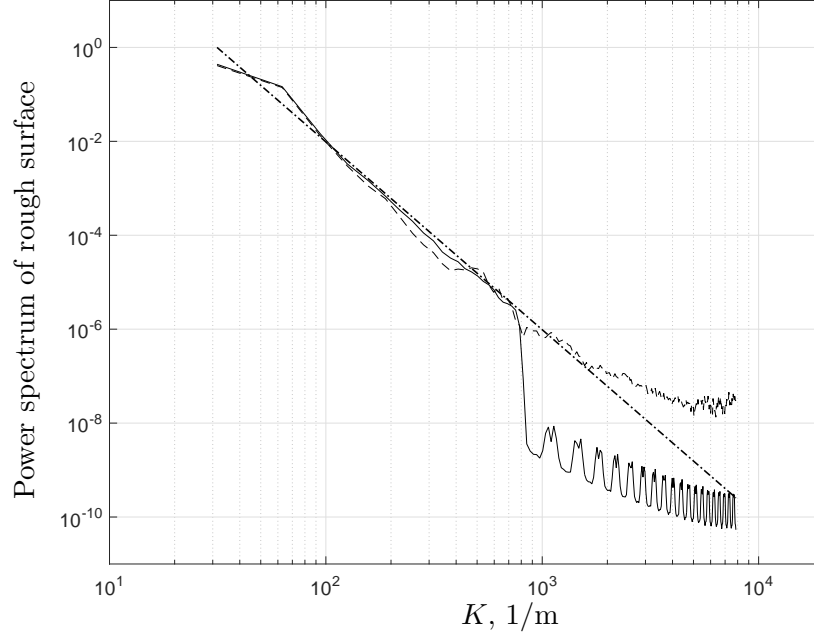


Figure 5: The normalized power spectrum averaged over 100 surface elevation realizations. Dash-dot line - the spectrum based on equation (27); dashed line - the inverted spectrum; solid line - the spectrum of the surfaces generated with equation (26).

255 agreement between the average spectrum inverted with the proposed technique and  
 256 that defined by equation (26) was within 15%.

## 257 **B Measured roughness**

258 In order to illustrate the application of the inversion method developed in Section III  
 259 we used the acoustic pressure data  $\mathbf{P}_{N \times 1}$  calculated with the Kirchhoff approximation  
 260 and with the full-wave 2-D FDTD method [13] for a range of roughness realizations  
 261 measured with the light-induced fluorescence method detailed in [9]. In the case of  
 262 the Kirchhoff approximation the acoustic pressure was calculated as described in the



263 previous section.

264 In the case of the FDTD method the acoustic pressure was computed for a source  
265 with directivity pattern defined by (25). This source directivity was simulated by  
266 setting up a 33 mm long line array of 49 point sources operated in phase. The  
267 frequency of the acoustic wave emitted by the source was  $f = 43$  kHz. The time and  
268 space discretization intervals in the FDTD calculations were  $1.03 \mu\text{s}$  and  $0.5$  mm,  
269 respectively.

270 The surface roughness data used in this work were obtained in a hydraulic flume  
271 with the method detailed in [9]. The flume had a bed of hexagonally packed spheres  
272 with a diameter of 25 mm, and was tilted to a slope of  $S_0 = 0.004$ . The flow was  
273 turbulent, uniform and constant velocity was maintained across the length of the  
274 measured spatial interval. The surface elevation data was collected for four flow  
275 regimes which corresponded to the flow with 60, 70, 80 and 90 mm of uniform water  
276 depth, respectively. These regimes corresponded to the mean flow velocity of 0.43,  
277 0.50, 0.57 and 0.65 m/s, respectively. The arrangement of the receiver positions in  
278 the models was identical to that detailed in the previous section.

279 In Figure 6 the real and imaginary parts of the angular dependent acoustic pres-  
280 sure predicted with the FDTD method is compared against that predicted with the  
281 Kirchhoff approximation (8). These results correspond to a realistic flow surface  
282 roughness realization measured for 60 mm deep flow regime. The results suggest  
283 that the Kirchhoff approximation generally underpredicts the acoustic pressure in  
284 comparison to that predicted by the FDTD method. This is particularly notice-  
285 able in the case of the imaginary part and for the angles of incidence close to  $45^\circ$ .  
286 These acoustic pressure data were then used with the proposed inversion technique  
287 to reconstruct the flow surface roughness.

288 Figures 7 (a)-(d) present the results of the application of the inverse technique

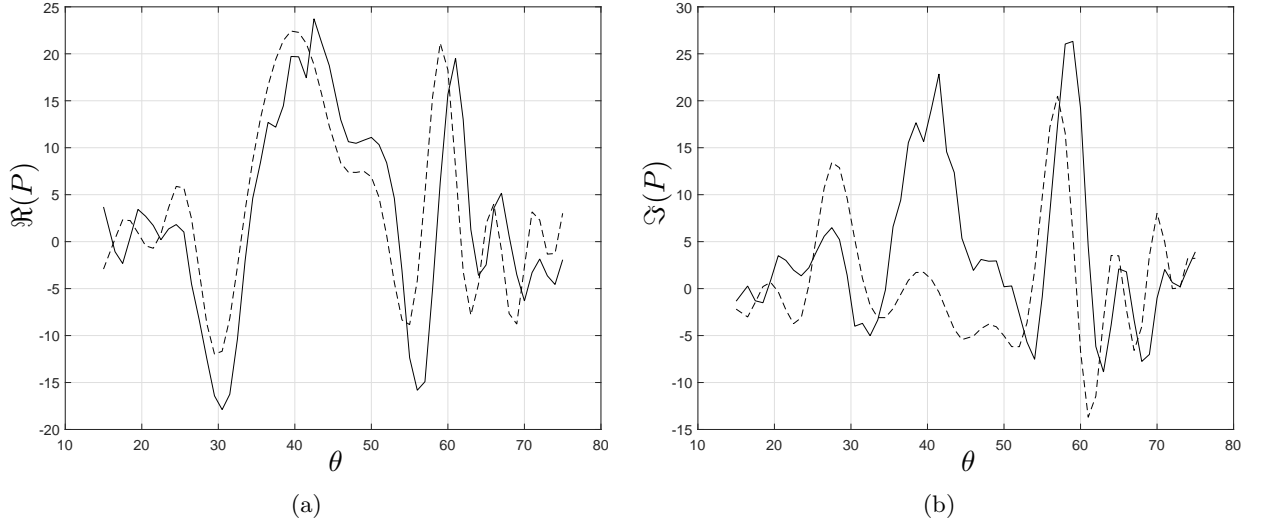


Figure 6: The scattered acoustic pressure for a single realization of the rough surface elevation for flow depth 60 mm predicted with FDTD method(solid line) and Kirchhoff approximation (8) (dashed line). (a) Real part, (b) imaginary part.

to the acoustic pressure data predicted with the Kirchhoff approximation and with the FDTD method for flow surface realizations representing each of the four flow regimes. The inversion results are shown in the range  $-0.1 < x < 0.1$  m where the maximum relative error was within 45% when the acoustic pressure was predicted with the FDTD method and 20% when the acoustic pressure was predicted with the Kirchhoff approximation. Within this interval the effects of shadowing and multiple scattering are relatively small that enables us to use equation (8) as an accurate approximation to the full-wave FDTD results. In all cases the minimum of  $\beta$  was in the interval  $[0, 1]$  and its values is listed in Table 1. The accuracy we achieved depended on how far the point on the surface was from the nominal specular reflection point.

Figure 8 presents the mean spatial spectra which demonstrate the range of scales

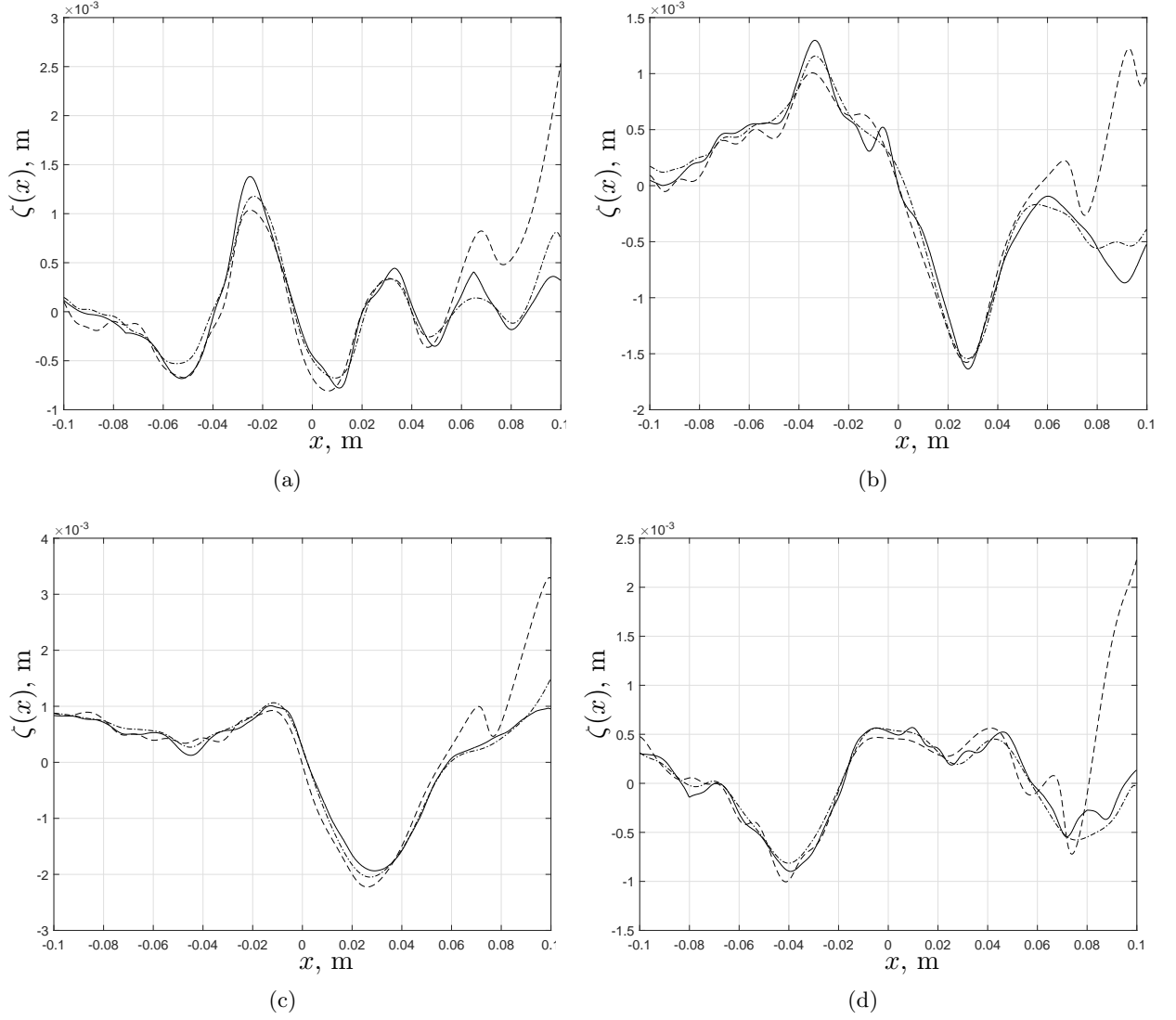


Figure 7: Examples of the surface elevation  $\zeta(x)$  for the four flow regimes. Solid line - measured with the LIF method; dashed line - reconstructed with the sound pressure data predicted with the FDTD mode; dashed-dot line - reconstructed with the acoustic pressure data predicted with the Kirchhoff approximation. (a) Flow depth 60 mm, (b) flow depth 70 mm, (c) flow depth 80 mm, (d) flow depth 90 mm.

301 of roughness which were recovered through the proposed inversion technique. These  
 302 spectra were inverted using the acoustic pressure data predicted with the Kirchhoff  
 303 approximation and with the FDTD method. As it was noted in the previous section  
 304 IV A, the normalized power spectrum provides information on the contribution of  
 305 different roughness scales to the pattern of waves observed on the surface. For the  
 306 four flow regimes considered in this work the recovered surface predicts the actual  
 307 slope of the power spectrum closely for  $K < 1000$  1/m. However, it is clear that for  
 308  $K > 1000$  1/m the proposed inversion techniques fails to identify the correct range  
 309 of roughness scales, i.e. those scales which are at a  $l_n < 6.3$  mm spatial wavelength.  
 310 This can be explained by the limitations of the Kirchhoff approximation (equation  
 311 (8)) as the local radius of curvature increases with the decrease of the surface scales.

312 It is difficult to obtain a useful measure of the error between the measured spec-  
 313 trum and that reconstructed with the proposed inversion method by comparing these  
 314 spectra directly. This is because the spectral power shown in Figure 8 varies by 10  
 315 orders of magnitude over the considered range of wavenumbers. For this purpose we  
 316 used the error estimate based on the difference in the values of the coefficients in  
 317 a functional fit which can be found to accurately represent the power spectrum as  
 318 suggested in Section 3 in [14]. For this purpose we adopted the following function

$$\log_{10} \tilde{S}(K) = 1/\{a + b \log_{10}^2(K)\}, \quad (29)$$

319 where  $a$  and  $b$  are some coefficients which can be adjusted to fit the data in the least  
 320 mean square sense, and  $\tilde{S}(K)$  is the power spectrum. Figure 9 shows two examples of  
 321 this spectral fitting for the 60 mm (a) and 90 mm (b) flow regimes. In the both cases  
 322 the coefficient of determination was  $R^2 > 0.98$ . The adopted values of the coefficients  
 323 in this fitting procedure were  $a = -0.0815$ ,  $b = 0.00478$  for the 60 mm flow regime  
 324 and  $a = -0.0840$ ,  $b = 0.00498$  for the 90 mm flow regime. These were obtained

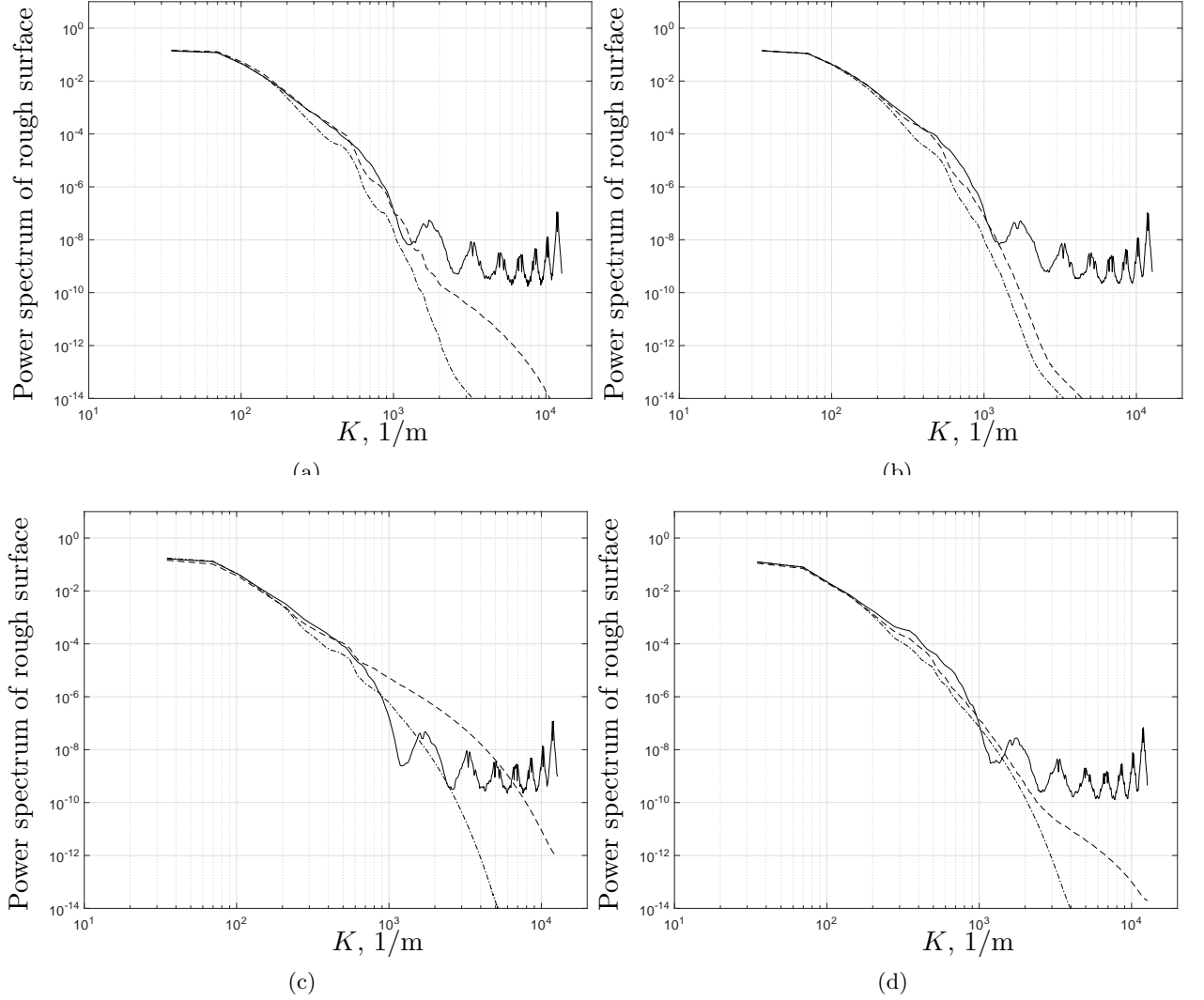


Figure 8: The normalized power spectrum of rough surface (solid line) compared against the power spectrum of the reconstructed surface where dashed and dashed-dot lines represent the use of FDTD and Kirchhoff approximation data, respectively. (a) Flow depth 60 mm, (b) Flow depth 70 mm, (c) Flow depth 80 mm, (d) Flow depth 90 mm.

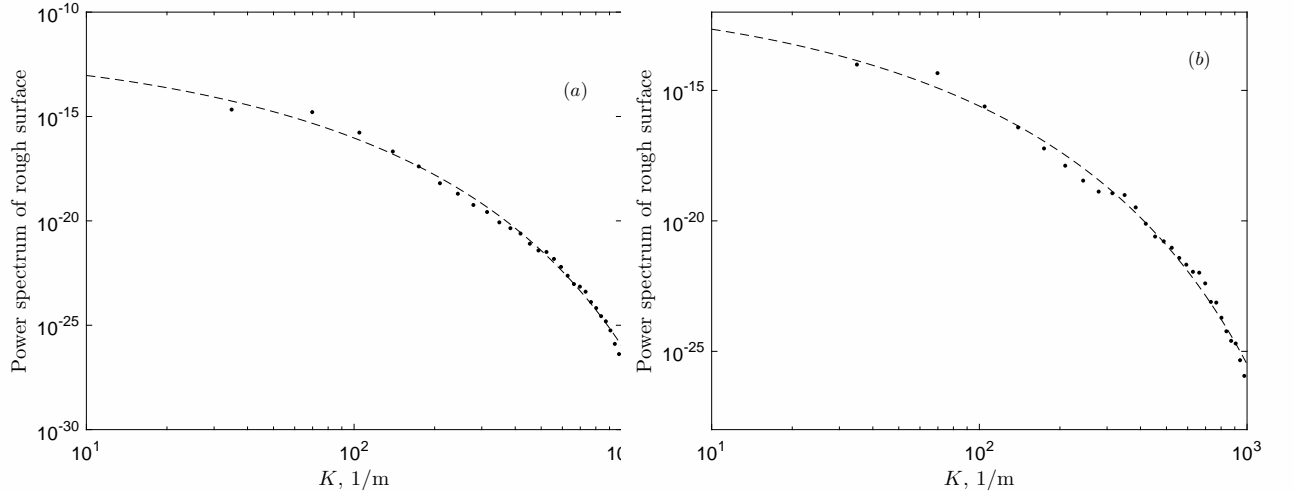


Figure 9: Examples of the measured power spectrum of the surface roughness (dots) and its fit with function (29) (dashed line). (a) Flow depth 60 mm, (b) Flow depth 90 mm.

325 for the range of  $30 < K < 1000$   $1/m$ . The proposed function fitting procedure  
 326 enabled us to estimate the differences between the spectra in terms of the values of  
 327 the coefficients  $a$  and  $b$  which need to be adopted to represent the power spectrum in  
 328 a subsequent analysis. A comparison of the fitted measured spectra and two spectra  
 329 recovered with the proposed acoustic method suggests that in the case of the 60 mm  
 330 and 90 mm flow regimes the relative difference between the coefficients  $a$  is within  
 331 2%. For these two regimes the relative difference between the coefficients  $b$  is within  
 332 7%. The maximum difference of 49% for the coefficients  $b$  is found between the fitted  
 333 measured spectrum and the spectrum recovered using the FDTD data obtained in  
 334 the case of the 80 mm flow regime. In the other cases this difference is below 10%.

## V Conclusion

In this paper we demonstrate the derivation of an inversion method based on the Kirchhoff approximation of the boundary integral equation and the application of an inverse technique based on SVD and Tikhonov regularization to an underdetermined system of equations. The surface roughness data we used in our work were simulated surface roughness and surface roughness measured with the LIF method. The proposed inversion method enables us to determine the 1-D surface roughness with a maximum rms error of 45% (FDTD method) and 20% (Kirchhoff approximation), both being sub-millimeter scale errors. This method also enables us to estimate the average spatial power spectrum of the surface roughness for the range of wavenumbers  $K < 1000$  1/m. This corresponds to spatial wavelengths of  $l_n > 3.5$  mm. This spectrum converges to its true mean value to within 15% provided that at least 100 realizations are used in the averaging process. The area of the rough surface which can be reconstructed with the proposed acoustic setup and with the reported accuracy is within  $\pm 0.1$  m range. This range determines the maximum wavelength in the spatial spectrum of surface which can be estimated with the proposed inversion method and it is limited by the number of the receivers in the microphone array and by the adopted directivity of the sound source. In the case when the surface roughness spectrum does not follow a power law, the errors were estimated using a function fitting procedure. The maximum error between the coefficients in the function fitting procedure was found 49% for the 80 mm flow regime. For other flow regimes considered in this work the relative error was below 10%.

The inversion method requires further improvements to increase accuracy for the scales in the centimeter and sub-centimeter range of spatial wavelength. This should involve the use of an extension of Kirchhoff approximation which can account

360 for higher roughness slopes or a more refined 3D numerical model. The retrieved  
361 roughness profiles can be used to find key statistical and spectral characteristics of  
362 the water surface. The proposed method can potentially be used together with the  
363 acoustic array measurements to accurately retrieve the temporal and spatial profile  
364 of the dynamic shallow water flow.

## 365 Acknowledgments

366 The authors are grateful to Dr. Andrew Nichols (University of Sheffield) for the  
367 provision of the LIF data some of which we used for the analysis reported in Section  
368 IV B.

## 369 References

- 370 [1] R.J. Wombell and J.A. DeSanto, "The reconstruction of shallow rough-surface  
371 profiles from scattered field data," *Inverse Problems*, 7, 7–12 (1991).
- 372 [2] S.P. Walstead and G.B. Deane, "Reconstructing surface wave profiles from re-  
373 flected acoustic pulses," *J. Acoust. Soc. Am.*, 133, 604-613 (2013).
- 374 [3] A. Krynkin, K. V. Horoshenkov, A. Nichols and S. J. Tait, "A non-invasive  
375 acoustical method to measure the mean roughness height of the free surface of a  
376 turbulent shallow water flow," *Review of Scientific Instruments*, 85 (11), 114902,  
377 (2014).
- 378 [4] A. Ishimaru, *Wave Propagation and Scattering in Random Media* (Academic  
379 Press, Inc., New York, 1978), pp. 484–487.



- [5] E.I. Thorsos, "The validity of the Kirchhoff approximation for rough surface scattering using a Gaussian roughness spectrum," J. Acoust. Soc. Am., 83, 78–92 (1988).
- [6] F. G. Bass and I. M Fuks, *Wave Scattering from Statistically Rough Surfaces* (Pergamon Press, Ltd, Oxford, 1979), p. 228.
- [7] W. H. Press, S. A. Teukolsky, W. T. Vetterling and B. P. Flannery, *Numerical Recipes: The Art of Scientific Computing* (3rd Edition, Cambridge University Press, Cambridge, 2007), pp. 65–75.
- [8] H.W. Engl, M. Hanke and A. Neubauer, *Regularization of Inverse Problems*, (Kluwer Academic Publ., Dordrecht, 2000), pp. 221–237.
- [9] A. Nichols, *The Interaction Mechanism of Airborne Acoustic Fields with Turbulent Shallow Flows* (Ph.D. thesis, University of Bradford, UK, 2014), pp. 76–79.
- [10] Q. Leclère, "Acoustic imaging using under-determined inverse approaches: Frequency limitations and optimal regularization", J. Sound Vib., 321, 605–619, (2009).
- [11] J.A. Toporkov and G.S. Brown, Numerical Simulations of Scattering from Time-Varying, Randomly Rough Surfaces, IEEE T. Geosci. Remote, 38, 1616–1625 (2000).
- [12] O. M. Phillips, "On the generation of waves by turbulent wind," J. Fluid Mech., 2, 417–445 (1957).
- [13] T. Van Renterghem, "Efficient outdoor sound propagation modeling with the finite-difference time-domain (FDTD) method: a review," Int. J. Aeroacoustics, 13 (5-6), 385-404 (2014).

- 403 [14] K. V. Horoshenkov, A. Nichols, S. J. Tait, G. A. Maximov, The pattern of  
404 surface waves in a shallow free surface flow, J. Geoph. Res., 118, 1–13 (2013).

Table 1: Examples of the minimum values of the regularization parameter  $\beta$  obtained for 4 realizations of the surface elevation associated with the four adopted flow regimes.

	60 mm	70 mm	80 mm	90 mm
$\beta \times 10^7$	8.4	8.4	8.4	13

## 406 List of figures

407 Figure 1. The geometry of the acoustic problem of rough surface scattering.

408 Figure 2. The acoustic setup used to reconstruct the rough surface in the numerical  
409 experiment.

410 Figure 3. (a) An example of the surface realization,  $\zeta(x)$ , (dashed line) used in  
411 equation (8) and its reconstruction from the Kirchhoff approximation (solid line)  
412 based on equation (23). (b) Absolute error of the reconstructed surface.

413 Figure 4. An example of the behavior of the function  $F(\beta)$  for the range of  
414  $10^{-20} < \beta < 10^5$ .

415 Figure 5. The normalized power spectrum averaged over 100 surface elevation  
416 realizations. Dash-dot line - the spectrum based on equation (27); dashed line - the  
417 inverted spectrum; solid line - the spectrum of the surfaces generated with equation  
418 (26).

419 Figure 6. The scattered acoustic pressure for a single realization of the rough  
420 surface elevation for flow depth 60 mm predicted with FDTD method(solid line)  
421 and Kirchhoff approximation (8) (dashed line). (a) Real part, (b) imaginary part.

422 Figure 7. Examples of the surface elevation  $\zeta(x)$  for the four flow regimes. Solid  
423 line - measured with the LIF method; dashed line - reconstructed with the sound  
424 pressure data predicted with the FDTD mode; dashed-dot line - reconstructed with  
425 the acoustic pressure data predicted with the Kirchhoff approximation. (a) Flow  
426 depth 60 mm, (b) flow depth 70 mm, (c) flow depth 80 mm, (d) flow depth 90 mm.

427 Figure 8. The normalized power spectrum of rough surface (solid line) compared  
428 against the power spectrum of the reconstructed surface where dashed and  
429 dashed-dot lines represent the use of FDTD and Kirchhoff approximation data,  
430 respectively. (a) Flow depth 60 mm, (b) Flow depth 70 mm, (c) Flow depth 80  
431 mm, (d) Flow depth 90 mm.

432 Figure 9. Examples of the measured power spectrum of the surface roughness  
433 (dots) and its fit with function (29) (dashed line). (a) Flow depth 60 mm, (b) Flow  
434 depth 90 mm.